Comparison of Longwave Infrared Hyperspectral Target Detection Methods

Seung Hwan An, Nathan P. Wurst, Joseph Meola
Air Force Research Laboratory
UNITED STATES OF AMERICA

ABSTRACT

Numerous methods exist to perform hyperspectral target detection. Application of these algorithms often requires the data to be atmospherically corrected. Detection for longwave infrared data typically requires surface temperature estimates as well. This work compares the relative robustness of various target detection algorithms with respect to atmospheric compensation and target temperature uncertainty. Specifically, the adaptive coherence estimator and spectral matched filter will be compared with subspace detectors for various methods of atmospheric compensation and temperature-emissivity separation. Comparison is performed using both daytime and nighttime longwave infrared hyperspectral data collected at various altitudes for various target materials..

1. INTRODUCTION

Longwave infrared (LWIR) hyperspectral imaging (HSI) has shown utility in detecting minerals and gaseous effluents with spectral features in the 7-14µm wavelength range. These sensors have the advantage of operating in the day or at night because they measure emitted and reflected thermal energy instead of sunlight. The sensor-measured radiance and surface emissivity must be known or estimated to perform target detection or material identification.

Processing of LWIR HSI data often handles the problems of atmospheric compensation (AC) and emissivity estimation separately. The majority of AC algorithms utilize either in-scene methods1, 2 or radiative transfer models[3–5] to estimate path transmission, upwelling radiance, and downwelling radiance (TUD) associated with the data. Upon obtaining atmospheric estimates, one can perform temperature-emissivity separation (TES) on the data to obtain emissivity estimates for use in sub- sequent matched target detection exploitation.

Target detection algorithms are applied in conjunction AC and TES to find materials of interest within a scene. Two common algorithms referred to as the adaptive coherence estimator (ACE) and spectral matched filter (SMF) can be applied in either the emissivity domain or the radiance domain.[6–8] Other subspace detection algorithms have been developed for application in the radiance domain to account for target/background variability and to alleviate the need to estimate emissivity for the entire data cube.

This research examines various combinations of AC, TES, and detection algorithms to assess robustness over a range of data cubes collected at different altitudes, cloud conditions and day/night for a number of different target materials. Section 2 discusses the airborne data used for the study as well as the specific AC, TES, and detection algorithms applied. Section 3 provides the detection results in terms of receiver operating characteristic (ROC) curves, signal-to-clutt**er ratio (SCR) and false alarms**

2. METHODOLOGY

The LWIR HSI data used for this study was collected using the Spatially Enhanced Broadband Array Spectrograph (SEBASS) sensor mounted on an aircraft operating at altitudes between 1500’ to 9000’ above ground level (AGL).[9] Five targets are chosen for this analysis with varying levels of spectral signature

strength. These targets correspond to a commercial foamboard material, a low emissivity paint (Low-E), and a medium emissivity paint (Mid-E), glass, and sandpaper with their measured spectral emissivity shown in Figure 1.

Table 1: Data summary

Datacube	Sky condition	Time-of-day	Altitude (AGL)
1	Clear	Afternoon	9000’
2	Clear	Afternoon	3000’
3	Clear	Afternoon	1500’
4	Partly cloudy	Morning	4000’
5	Partly cloudy	Morning	6000’
6	Clear sky	Nighttime	3000’
7	Clear sky	Nighttime	1500’
8	Cloudy	Afternoon	1500’
9	Cloudy	Afternoon	3000’

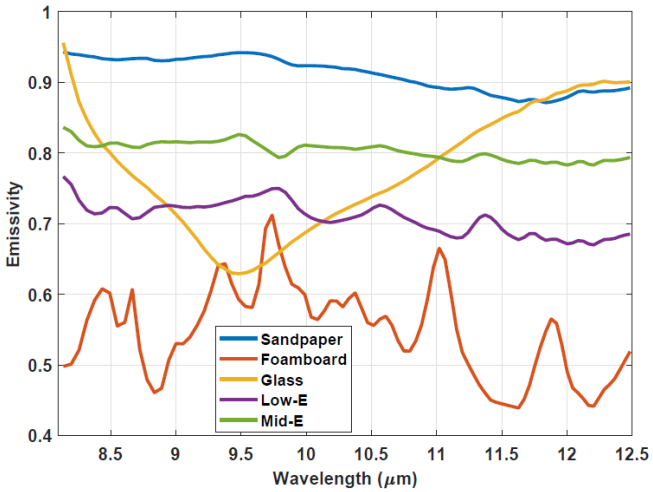

Figure 1: Measured target spectral emissivity

A simple model for sensor-reaching radiance in the LWIR is given by

$$L(\lambda) = L_u(\lambda) + \left[L_d(\lambda)(1-\epsilon(\lambda)) + \epsilon(\lambda)B(\lambda,T)\right]\tau(\lambda) \quad (1)$$

where $L_u(\lambda)$ is the upwelling radiance, $L_d(\lambda)$ is the downwelling radiance, $\tau(\lambda)$ is atmospheric path transmission, $\epsilon(\lambda)$ is emissivity, and $B(\lambda,T)$ is the radiance of a blackbody at temperature T.8 The process of atmospheric compensation seeks to estimate the transmission, upwelling, and downwelling (TUD) components of this model. Five different AC methods are used in this analysis, all of which utilize MODTRAN or a similar radiative transfer tool to generate TUD estimates. The methods used include:

1. **MODTRAN (MOD):** Simple MODTRAN simulation using known sensor altitude, band centers, band widths, and assuming mid-latitude summer atmospheric model.

2. **FLAASH-IR (FLA):** Algorithm using MODTRAN with known sensor altitude, band centers, band widths with an optimization procedure for water vapor, temperature, and ozone profiles to reduce fit

error.4

3. **NOMADS (NOM):** Algorithm using MODTRAN with known sensor altitude, band centers, band widths, and using numerical weather prediction data obtained from the National Oceanic and Atmospheric Administration (NOAA) Operational Model Archive Distribution System (NOMADS).[5, 10]

4. **AFRL-1:** Experimental AFRL method using MODTRAN and concepts similar to FLAASH- IR.

5. **AFRL-2**: Experimental AFRL method using alternative radiative transfer modeling and concepts similar to FLAASH-IR.

Several data transformations are used in this study that strive to bring the data and target signature into the same domain in order to permit target detection. One method is conversion of the radiance data cube to emissivity space. Given TUD estimates, conversion to emissivity requires a temperature estimate for each data pixel. While this approach can be effective, it is also computationally demanding. An alternative method referred to as the alpha-residuals (AR) transform applies a mathematical manipulation to the data using a couple of simplifying assumptions.

As an alternative to converting the data to emissivity space, the target signature can be converted to radiance space for target detection purposes. Given TUD estimates, one must choose a target temperature in order to generate the target radiance signature. A simple approach is to assume the target temperature will be close to the ground temperature. An approximate ground temperature can be obtained for near-blackbody background materials by selecting the maximum apparent spectral temperature (AST) of the mean background radiance from the scene after converting to ground-leaving radiance.[8]

To limit detection performance losses resulting from an inaccurate target temperature estimate, a target signature subspace can be generated. Given accurate TUD estimates, a target radiance subspace can be generated by modeling many realizations of the same target over a wide temperature range and performing a singular value decomposition (SVD) on the resulting data to obtain basis vectors describing the linear subspace.[9]

The methods applied for this study are summarized below.

1. **Max-smoothness algorithm (MSA):** Convert data cube to emissivity space using TUD estimates with max-smoothness algorithm.[11]

2. **Alpha Residuals-1 (AR-1):** Emissivity estimate derived from alpha residual transform.[12]

3. **Alpha Residuals-2 (AR-2):** Emissivity estimate derived from modified alpha residual transform.[13]

4. **Apparent Spectral Temperature (AST):** Convert target emissivity to radiance domain using TUD estimates and temperature estimate obtained from maximum AST of the mean background after conversion to ground-leaving radiance.

5. **Target subspace generation (only for subspace detectors):** Generate target radiance signatures over a temperature range and determine subspace using SVD.

Several detection algorithms are examined in this work to test relative robustness with respect to TUD estimates and emissivity/signature estimates. ACE and SMF are two signature-matched detectors which the data can be in 1) emissivity space (using MSA), 2) radiance space (using AST), or 3) emissivity derived from alpha-residuals space (using AR-1 or AR-2).[14] The subspace detectors examined here include subspace ACE

(ssACE), joint subspace detector (JSD), and adaptive subspace detector (ASD).[14] For this work, the background subspace matrix is obtained using the leading ten eigenvectors of the scene sample covariance matrix

3. RESULTS

The various combinations of AC, emissivity retrieval, and detection algorithms are applied to the data sets with results summarized below. Due to the large number of combinations examined, example cases are shown and total results are summarized in tabular form. Example results of TUD and emissivity estimates can be found in the associated reference.[14]

Various performance metrics are examined here, including receiver operating characteristic (ROC) curves, signal-to-clutter (SCR) ratio and number of false alarms (FAs) at a given probability of detection (Pd). For a single data cube and a single target material, 55 different combinations of AC, TES, and detection algorithms exist. Having examined 9 data cubes and 5 targets, a total 2,475 detection results were produced. Example ROC curves are shown in Figure 2 for the sandpaper, mid-E, and foamboard target materials for all 55 combinations of algorithms using the same data cube. These targets are selected to range across easier (foamboard) and more challenging (sandpaper) to detect. The area under curve (AUC) is computed for each case and the minimum, median, and maximum curves are highlighted. In this example, the ACE and SMF algorithms tend to outperform the subspace methods for all targets. Additionally, lower variability in detection performance is observed for the easier foamboard target material.

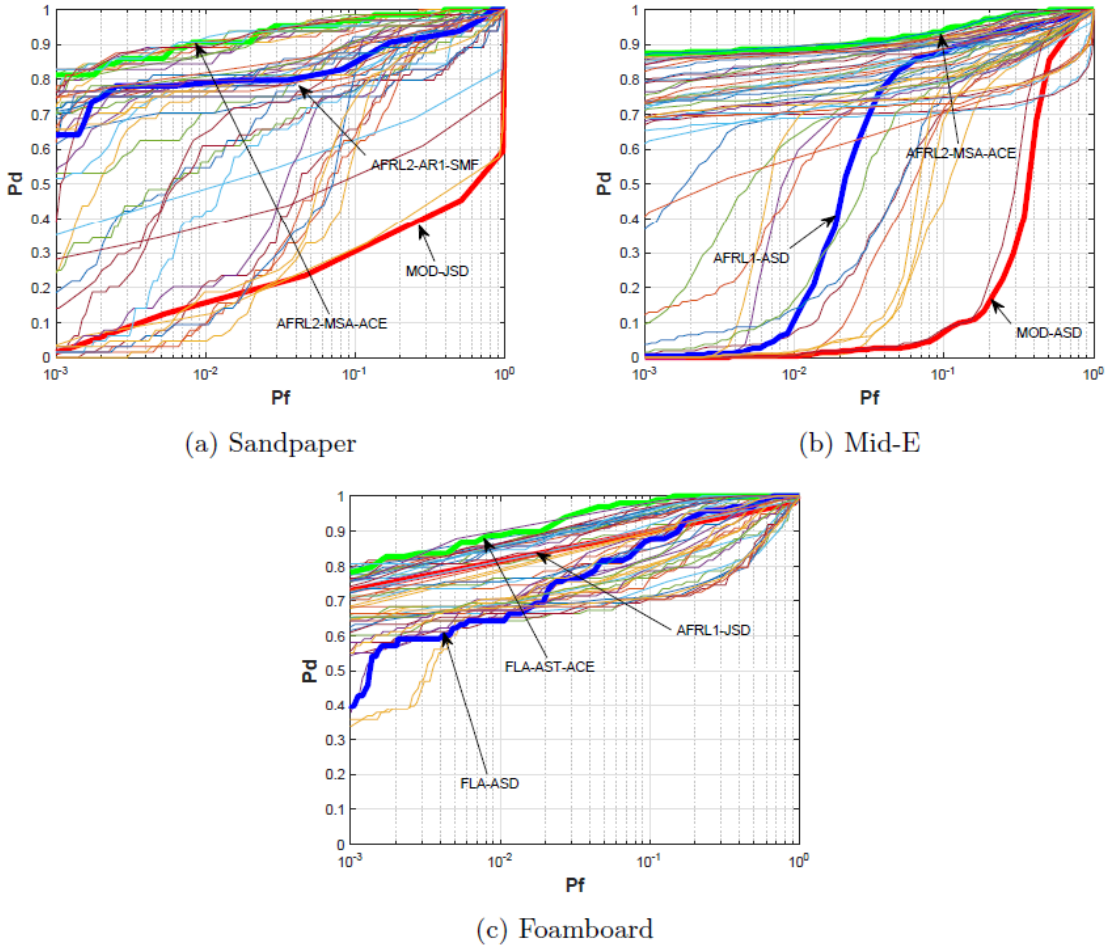

Figure 2: Comparison of ROC curves for various methods

SCR and FA metrics are used to summarize results over all data cubes and targets. The FAs are computed for a probability of detection of 0.5. To summarize all 2,475 results, the SCR and FA were computed by averaging over all targets and data cubes for each AC, TES and detection algorithm.

Table 2 shows the SCR scores for the ACE detection algorithm for all combinations of AC and TES algorithms averaged over all data cubes. In this case, the combination of FLAASH-IR with AST

appears to provide the best overall performance for ACE in terms of SCR. Additionally, the average performance for each target suggests sandpaper is the most difficult to detect while foamboard is the easiest.

Due to the nature of the detection algorithms (linear vs. quadratic, subspace, etc.), direct com- parison of SCR does not necessarily directly correlate to relative detection performance. As such, the normalized SCR is used to provide a relative comparison of which AC-TES combination tends to achieve the highest average performance for each detection algorithm. Table 3 displays the av- erage normalized SCR for each detection algorithm over all data cubes and all targets. Again, the FLAASH-AST combination demonstrates the best average SCR performance for both ACE and SMF. No clear trends are apparent for the subspace-based detection algorithms.

To provide a more direct comparison of detection performance between algorithms, a FA metric is used.

Table 4 provides average FAs over all data cubes for the ACE algorithm for each target. The combination of AFRL-2 and AST produces the lowest average FAs. However, the FA performance for FLAASH-AST is comparable and a correlation exists between SCR and FAs. Table 5 displays the average FAs for all algorithms over all targets and data cubes. Again, the lowest average FAs result from the combination of AFRL-2 and AST although the FLAASH-AST combo is comparable. The ACE algorithm produces the lowest FAs overall for the best AC-TES combination. However, it is worth noting that for many other "non-optimal" combinations, SMF produces fewer FAs. This suggests that SMF is a bit more robust than ACE to target signature mismatch as the FAs for ACE can grow quickly if a sub-optimal signature is used. The subspace methods tend to produce a much larger number of FAs with ssACE producing the fewest within this class of algorithm.

Finally, detection performance as a function of data cube is examined. Figure 3 displays nor- malized average SCR and FAs for each data cube for each AC method where the average is taken over all detection algorithms, TES methods, and targets. In general, detection performance drops considerably for the nighttime data, most likely due to reduced contrast due to thermal equilibrium and lower signal levels due to reduced temperature. Cloud cover appears to reduce performance in some cases as well

4. CONCLUSIONS

This work attempts to compare different combinations of AC, TES and detection algorithms to assess robustness with respect to operating altitude, time of day, weather conditions, and target material. General trends noted superior performance using some combination of FLAASH-IR or AFRL-2 methods for AC and MSA or AST for TES. In all combinations, it is clear that all algo- rithms deteriorate for nighttime conditions. Future work should continue to expand this study to various sensors, backgrounds, and target types

.

ACE	MOD MSA	MOD AR1	MOD AR2	MOD AST	AFRL 1 MSA	AFRL 1 AR1	AFRL 1 AR2	AFRL 1 AST	NOM MSA	NOM AR1	NOM AR2	NOM AST	FLA MSA	FLA AR1	FLA AR2	FLA AST	AFRL 2 MSA	AFRL 2 AR1	AFRL 2 AR2	AFRL 2 AST	Average
Sandpaper	2.45	1.62	2.71	2.37	3.75	1.77	3.22	4.39	2.12	1.99	3.10	2.41	3.65	1.76	3.84	4.44	3.72	2.10	3.80	4.64	2.99
Foamboard	8.04	3.58	4.33	7.46	8.06	3.62	5.07	7.50	8.32	3.20	4.33	7.71	8.62	4.03	5.04	8.47	8.47	3.64	4.89	7.85	6.11
Glass	5.79	5.72	4.90	5.60	6.19	5.52	4.93	6.35	5.60	5.77	5.22	5.90	6.05	5.53	4.88	6.41	6.02	5.46	5.22	6.16	5.66
Low-E	5.86	1.86	3.68	6.26	7.19	2.77	4.20	6.82	5.90	2.05	3.18	6.81	7.91	2.97	3.91	8.59	7.72	2.87	3.82	7.48	5.09
Mid-E	3.14	0.71	2.09	3.22	5.20	1.00	2.91	5.25	2.87	0.97	1.72	3.25	5.39	0.96	2.81	6.31	5.44	1.73	2.34	5.37	3.14
Average	5.06	2.70	3.54	4.98	6.08	2.93	4.06	6.06	4.96	2.80	3.51	5.22	6.33	3.05	4.10	6.84	6.27	3.16	4.01	6.30	-

Table 2: The averaged SCR over all data cubes for each AC and TES method using the ACE detection algorithm. The green highlighted blocks represent the highest SCR of all methods for each target

Normalized SCR	MOD MSA	MOD AR1	MOD AR2	MOD AST	AFRL 1 MSA	AFRL 1 AR1	AFRL 1 AR2	AFRL 1 AST	NOM MSA	NOM AR1	NOM AR2	NOM AST	FLA MSA	FLA AR1	FLA AR2	FLA AST	AFRL 2 MSA	AFRL 2 AR1	AFRL 2 AR2	AFRL 2 AST
SMF	0.79	0.43	0.53	0.78	0.93	0.51	0.63	0.91	0.80	0.43	0.51	0.84	0.96	0.54	0.62	1	0.98	0.55	0.63	0.95
ACE	0.74	0.39	0.52	0.73	0.89	0.43	0.59	0.89	0.72	0.41	0.51	0.76	0.92	0.45	0.60	1	0.92	0.46	0.59	0.92

Norm SCR	MOD	AFRL 1	NOM	FLA	AFRL 2
ssACE	0.84	0.89	0.84	0.91	1.00
JSD	0.89	1.00	0.91	0.88	0.98
ASD	0.76	0.80	0.75	1.00	0.76

Table 3: The normalized SCR of the averages of each detection algorithm for each AC and TES method.

ACE	MOD				AFRL 1				NOM				FLA				AFRL 2			
	MSA	AR1	AR2	AST	MSA	AR1	AR2	AST	MSA	AR1	AR2	AST	MSA	AR1	AR2	AST	MSA	AR1	AR2	AST
Sandpaper	26127	107109	5293	12093	968	86105	1848	80	27411	117863	2042	7513	2345	100034	270	127	922	100608	284	60
Foamboard	1	1365	248	1	1	3667	72	1	1	8046	81	1	1	2500	449	1	1	3583	133	1
Glass	83	57	205	66	38	47	149	39	46	58	181	49	51	41	231	48	51	52	142	33
Low-E	8	26862	308	3	1	3938	766	0	7	46094	892	0	6	18610	641	11	1	6519	1314	0
Mid-E	30953	133094	10440	13803	196	162571	33670	42	21257	139537	27809	3705	99	140729	5618	46	76	109926	31188	22
Average	11434	53698	3299	5193	241	51266	7301	32	9744	62320	6201	2254	500	52383	1442	47	210	44138	6612	23

Table 4: The averaged FA over all datacube for each AC and TES method using ACE detection algorithm. The green highlighted blocks represent the lowest FA of all method for each target. AFRL2-AST method has the lowest FA overall.

Average	MOD				AFRL 1				NOM				FLA				AFRL 2			
FA	MSA	AR1	AR2	AST	MSA	AR1	AR2	AST	MSA	AR1	AR2	AST	MSA	AR1	AR2	AST	MSA	AR1	AR2	AST
SMF	8361	46565	1036	1913	197	53007	5102	130	5951	57643	1490	1141	420	50944	608	145	148	45106	4904	118
ACE	11434	53698	3299	5193	241	51266	7301	32	9744	62320	6201	2254	500	52383	1442	47	210	44138	6612	23

Average	MOD	AFRL 1	NOM	FLA	AFRL 2
ssACE	3025	4243	8952	5975	1263
JSD	50354	36541	44538	42078	34947
ASD	23884	5779	19542	11731	27164

Table 5: The average FA of each detection algorithm for each AC and TES method. The green highlighted blocks represent the lowest FA count out of all AC and TES combination.

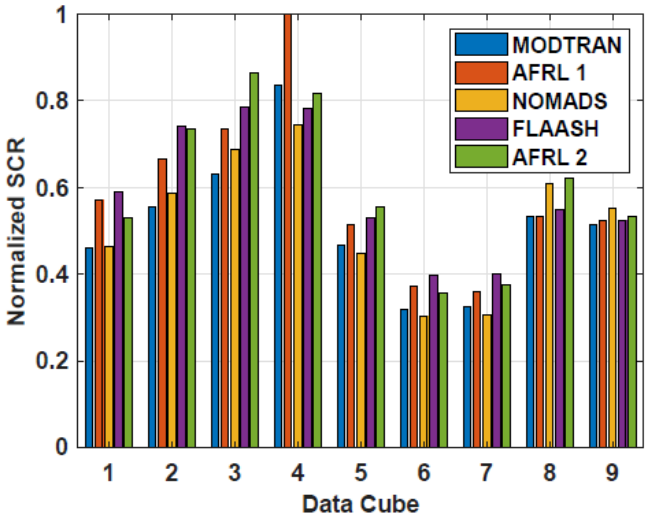

(a) Normalized SCR ratio for all datacube.

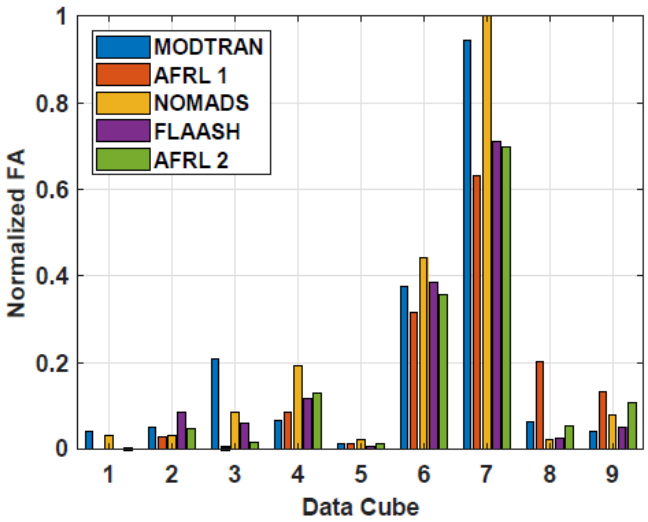

(b) Normalized FA for all datacube.

Figure 3: Comparison of SCR and FA of each datacube

REFERENCES

[1] R. J. DiStasio, Jr. and R. G. Resmini, "Atmospheric compensation of thermal infrared hy- perspectral imagery with the emissive empirical line method and the in-scene atmospheric compensation algorithms: a comparison," Proc. SPIE 7695, pp. 76952B–76952B–12, 2010.

[2] S. J. Young, B. R. Johnson, and J. A. Hackwell, "An in-scene method for atmospheric compensation of thermal hyperspectral data," Journal of Geophysical Research: Atmo- spheres 107(D24), pp. ACH 14–1–ACH 14–20, 2002.

[3] A. Berk, P. Conforti, and F. Hawes, "An accelerated line-by-line option for MODTRAN com- bining on-the-fly generation of line center absorption within 0.1 cm-1 bins and pre-computed line tails," Proc. SPIE 9472, pp. 947217–947217–11, 2015.

[4] S. M. Adler-Golden, P. Conforti, M. Gagnon, P. Tremblay, and M. Chamberland, "Long- wave infrared surface reflectance spectra retrieved from telops hyper-cam imagery," Proc. SPIE 9088, pp. 90880U–90880U–8, 2014.

[5] N. P. Wurst, J. Meola, and S. T. Fiorino, "Improved atmospheric characterization for hyper- spectral exploitation," Proc. SPIE 10198, p. 101980B, 2017.

[6] S. Kraut and L. Scharf, "The CFAR adaptive subspace detector is a scale-invariant GLRT," in Statistical Signal and Array Processing, 1998. Proceedings., Ninth IEEE SP Workshop on, pp. 57 –60, sep 1998.

[7] D. Manolakis, D. Marden, and G. A. Shaw, "Hyperspectral image processing for automatic target detection applications," Lincoln Laboratory Journal 14(1), pp. 79–116, 2003.

[8] M. T. Eismann, Hyperspectral Remote Sensing, SPIE, Bellingham, Washington, 2012.

[9] B. M. Rankin, J. Meola, D. L. Perry, and J. R. Kaufman, "Methods and challenges for target detection and material identification for longwave infrared hyperspectral imagery," 9840, 2016.

[10] G. K. Rutledge, J. Alpert, and W. Ebisuzaki, "NOMADS: A climate and weather model archive at the national oceanic and atmospheric administration.," Bulletin of the American Meteorological Society 87(3), pp. 327–341, 2006.

[11] C. Borel, "Error analysis for a temperature and emissivity retrieval algorithm for hyperspectral imaging data," Proc. SPIE 6565, pp. 65651Q–65651Q–12, 2007.

[12] P. S. Kealy and S. J. Hook, "Separating temperature and emissivity in thermal infrared mul- tispectral scanner data: implications for recovering land surface temperatures," IEEE Trans- actions on Geoscience and Remote Sensing 31, pp. 1155–1164, Nov 1993.

[13] M. Diani, M. Moscadelli, and G. Corsini, "Improved alpha residuals for target detection in thermal hyperspectral imaging," IEEE Geoscience and Remote Sensing Letters 15, pp. 779– 783, May 2018.

[14] N. P. Wurst, S. H. An, and J. Meola, "Comparison of longwave infrared hyperspectral target detection methods," Proc. SPIE 10986, 2019.

This information is furnished on the condition that it will not be released to another nation without specific authority of the Department of the Air Force of the United States, that it will be used for military purposes only, that individual or corporate rights originating in the information, whether patented or not, will be respected, that the recipient will report promptly the United States any known or suspected compromise, and that the information will be provided substantially the same degree of security afforded it by the Department of Defense of the United States. Also, regardless of any other markings on the document, it will not be downgraded or declassified without written approval from the originating US agency.